Check for updates

Gas-phase reactivity of hexanuclear molybdenum [Mo$_6$I$_{14}$]$^{2-}$ and its photo-fragments towards O$_2$ and CO$_2$: combined mass spectrometry (MS^n) and quantum chemical simulations†

Aikaterini Tsirkou,[a] Nina Tyminska,[bc] Richard A. J. O'Hair, [d] Fabien Grasset,[e] Yann Molard, [c] Karine Costuas, *[c] Stéphane Cordier *[c] and Luke MacAleese *[a]

The optical properties, photo-decomposition and photo-reactivity of [Mo$_6$I$_{14}$]$^{2-}$ clusters and their associated photo-products are examined in the gas phase. The UV-visible optical spectrum of the electron-rich [Mo$_6$I$_{14}$]$^{2-}$ cluster is measured and the wavelength dependence of the principal fragments is interpreted on the basis of the quantum chemistry (QC) simulated spectrum and detailed transitions. A special focus of attention is the photo-generated [Mo$_6$I$_{14}$]$^-$ and photo-specific radical [Mo$_6$I$_{13}$]$^{2-\bullet}$ as well as halogen-depleted clusters [Mo$_6$I$_n$]$^-$ with $n < 14$. The fragmentation and reaction energetics of all species are examined with a combination of mass spectrometry experiments, ion–molecule reactions with O$_2$ and CO$_2$ under irradiation and QC simulations. Reactions with O$_2$ are shown to be very exergonic with up to 5 eV release when O$_2$ is dissociated on the cluster. Experimental evidence for the photo-decomposition of CO$_2$ into CO and O on [Mo$_6$I$_n$]$^-$ ions is provided together with detailed QC energetics.

Introduction

Atomically precise metal nanoclusters display unique reactivity that cannot be inferred from either atomic or bulk matter. Their properties have been widely reviewed.[1] Among them, hexanuclear Mo$_6$ clusters are promising photocatalysts, reported for hydrogen evolution[2] and CO$_2$ photo-reduction.[3] Their robustness and stability make them sustainable alternatives to dye-based systems. Synthesized at high temperature and stabilized by halogen ligands (X), they form [{Mo$_6$X$^i_8$}X$^a_6$]$^{2-}$ building blocks, where face-capping (X^i) and terminal (X^a) ligands control optical and redox properties.[4,5] Ligand exchange enables integration in diverse matrices[4] or immobilization onto surfaces.[6–8] [Mo$_6$X$_{14}$]$^{2-}$ complexes exhibit broad

UV-vis absorption and strong red/NIR emission[5,9] making them attractive, less costly photo-sensitizers and catalysts. However, their precise reaction mechanisms, particularly under irradiation, remain poorly understood.

Mass spectrometry (MS) offers a complementary approach to solution studies by generating, isolating, and probing reactive intermediates at the molecular scale. Optical spectroscopy of mass-selected ions, using both UV-vis[10] and IR,[11] provides insight into transient species relevant for reactions in solution[12] in laser-ablation-generated gas-phase clusters. For metal and metal–oxide clusters, this approach has elucidated CO$_2$ coordination modes and proposed mechanisms for cluster-assisted reduction reactions.[11,13–20]

Although Mo$_6$ nanoclusters are established photocatalysts,[2,3] their gas-phase photo-reactivity is less explored. Warneke *et al.* investigated electrosprayed [Mo$_6$X$_{14}$]$^{2-}$ (X = halogen): photoelectron spectra revealed electron binding energies[21] while collision-induced dissociation (CID) showed halogen-radical loss and secondary reactivity with O$_2$.[22]

Here, we extend these pioneering studies to the photo-decomposition and photo-reactivity of Mo$_6$ clusters in the gas phase, focusing on [Mo$_6$I$_{14}$]$^{2-}$. Specifically, we ask the following: (i) do laser-induced dissociation (LID) pathways differ from CID pathways? (ii) What is the stability of photofragments? (iii) How do they react with O$_2$ or CO$_2$? (iv) How do binding sites, coordination, and radical/electron-acceptor character govern reactivity?

^{a} *Institut Lumière Matière, UMR5306 CNRS & UCBL, Lyon, France.*
  E-mail: luke.mac-aleese@univ-lyon1.fr

^{b} *Institute for the Sciences of Light, University Paris-Saclay, France*

^{c} *Institut des Sciences Chimiques de Rennes, UMR6226 CNRS & Université de Rennes, Rennes, France*

^{d} *School of Chemistry and Bio21 Institute of Molecular Science and Biotechnology, University of Melbourne, Victoria, Australia*

^{e} *CNRS–Saint-Gobain–NIMS, IRL3629, LINK, National Institute for Materials Science, Ibaraki, Japan*

† Dedicated with respect and admiration to Professor Helmut Schwarz on the occasion of his award of the Wolf Prize in Chemistry, an important recognition for his outstanding work on exploring reactive species in the gas phase to solve fundamental problems in catalysis.

23166 | *Phys. Chem. Chem. Phys.*, 2025, **27**, 23166–23178

This journal is © the Owner Societies 2025

Experiments are complemented by quantum-chemical (QC) simulations to characterize excitations, photofragment structures, stabilities, and reactivity with O_2 and CO_2. Ion–molecule reactions in an ion trap further provide mechanistic insight into these well-defined species.[23–25]

Experimental and theoretical methods

Synthesis

$Cs_2[\{Mo_6Br^i_8\}Br^a_6]$ and $Cs_2[\{Mo_6I^i_8\}I^a_6]$ were synthesized as described in ref. 26. Binary halides Mo_6Br_{12} and Mo_6I_{12} were first prepared using solid-state reactions of elemental precursors. Stoichiometric mixtures of CsX and Mo_6X_{12} were then sealed in quartz ampoules and heated to 850 °C (Br) or 700 °C (I). The resulting $Cs_2[\{Mo_6X^i_8\}X^a_6]$ complexes are soluble in water and organics, where labile X^a ligands can be exchanged with inorganic or organic groups (L). Cs^+ counterbalances the cluster charge.

Gas-phase experiments

All multi-stage (MSn) experiments were carried out using a modified a Thermo LTQ Velos ion trap mass spectrometer. $[Mo_6I_{14}]^{2-}$ was generated by electrospray ionization (ESI) of $Cs_2Mo_6I_{14}$ (1 μM, acetonitrile). CID of $[Mo_6I_{14}]^{2-}$ and product ions was performed in-trap and energy values are reported in instrument specific normalized collisional energy (NCE) units.[27] Single isotope peaks were isolated when possible; above m/z 2000, isolation windows included adjacent isotopes due to resolution limits. Assignments for fragment ions in Fig. 1, 6 and 11 are detailed in the SI Tables S1 and S2.

Optical spectroscopy

Optical action (fragmentation) spectra were obtained by irradiating mass-selected $[Mo_6I_{14}]^{2-}$ with single OPO laser pulses
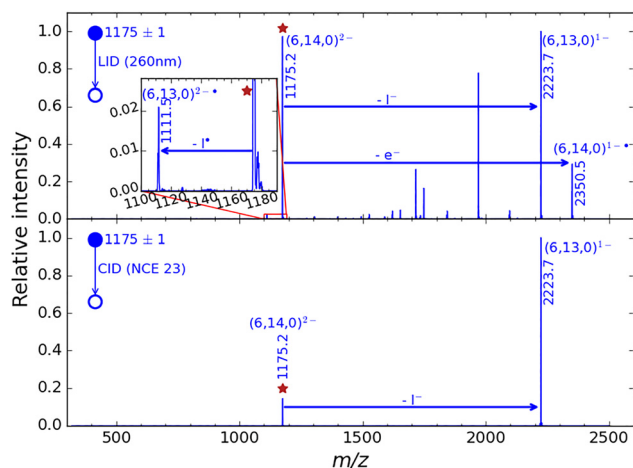

Fig. 1 (top) Photo-fragmentation spectrum (LID) at 260 nm and (bottom) collision-induced dissociation (CID) of a single isotopic peak (m/z 1175.2) of the precursor ion $(6,14,0)^{2-}$ denoted by a star (see the nomenclature section of fragments annotations). Both the oxidized (electron-photo-detached) $(6,14,0)^{1-}$ mono-anion species at m/z 2350.5 and the $(6,13,0)^{2-\bullet}$ dianionic species at m/z 1111.5 resulting from the $I^\bullet$ photo-cleavage are photo-specifically formed. Primary fragments are denoted with thick blue arrows. See SI Table S1 for details on assignments.

(200–600 nm, 2 nm steps). Laser power was tuned to keep fragmentation <1% at reference wavelengths (260, 340, and 540 nm). For each point, 200 mass spectra were averaged. Fragmentation ratios were normalized to laser power × wavelength and smoothed to yield fragmentation yields (details in SI Complement S3).

Photo-reactivity and ion–molecule reactions

$[Mo_6I_{14}]^{2-}$ precursors were mass-selected and irradiated (260 nm, 1 mJ, 5 ns pulses) to generate $[Mo_6I_{13}]^-$, $[Mo_6I_{13}]^{2-\bullet}$, or $[Mo_6I_{14}]^{-\bullet}$, which were isolated and monitored during MS^3. Helium buffer gas was seeded with O_2 or CO_2 (5000 ppm; estimated 840/67 and 910/73 collisions per second, respectively; see the SI). Reaction times were varied up to 10 s before MS acquisition. For photochemical studies, $[Mo_6I_9]^-$ was trapped in CO_2 and irradiated with a 488 nm CW laser (80 mW).

Simulations

Density functional theory (DFT) calculations were carried out using the Amsterdam Modeling Suite (AMS 2022.105)[28] driver with the Amsterdam Density Functional (ADF) engine.[29,30] The revPBE exchange-and-correlation functional[31,32] was employed to optimize all geometrical structures, to calculate electronic, vibrational and electronic excitation properties. Dispersion correction with the electronegativity equilibrium model developed by the Grimme group[33] was added. Due to the presence of heavy elements in the considered herein systems, the scalar relativistic effects have been included by using first-order perturbation theory from a ZORA Hamiltonian.[34] The all-electron quadruple-ζ Slater-type orbital basis set with the four polarization function (QZ4P) basis set implemented in the ADF was used. Vertical excitation energies were obtained using Tamm–Dancoff approximation (TDA-DFT).[35] Considering that the calculated systems are (doubly)-negatively charged, the conductor-like screening model[36] (COSMO) with a dielectric constant of 1.45 and the solvent radius of 2.36 Å (mimicking N_2) was applied to ensure that the energy of the occupied molecular orbitals are negative (see SI Complements S4). Vibrational frequency calculations were performed to ensure that the optimized structures are minima of the potential energy surface. The basis set superposition error was taken into account *via* the counterpoise correction while calculating the vertical bond dissociation energies.[37]

Nomenclature/terminology

Here, "cluster" denotes the Mo_6 octahedral unit; together with eight inner halogens it forms the "cluster core." The full motif, with apical ligands, is the "Mo_6 complex." Product ions are labeled by triplets (#Mo, #I, and #O) followed by charge. For example, $[Mo_6I_{14}]^{2-}$ and $[Mo_6I_{10}O_2]^{-\bullet}$ are denoted as $(6,14,0)^{2-}$ and $(6,10,2)^{1-\bullet}$.

Results and discussion

QC, CID *vs.* LID of the precursor $[Mo_6I_{14}]^{2-}$

Primary fragments and photo-specificity. CID of the face-capped $(6,14,0)^{2-}$ ion (single isotopic peak selected at m/z 1175) yields

This journal is © the Owner Societies 2025

Phys. Chem. Chem. Phys., 2025, **27**, 23166–23178 | **23167**

exclusively the singly charged $(6,13,0)^{1-}$ ion at m/z 2223 (see Fig. 1/bottom) by loss of iodide (I^-, with mass 126.9 Da). This is consistent with prior CID observations by Warneke and coworkers.[22] They additionally observed secondary losses of $I^\bullet$, although they remarked in their multi-instrument approach that "CID substantially varies among mass spectrometers". By contrast, the photo-activation (at 260 nm in Fig. 1/top) of $(6,14,0)^{2-}$ yields a much richer variety of ions. Among the photo-product ions, it is possible to identify three primary ions (thick blue arrows in Fig. 1 and Scheme 1): first, the electron detachment product $(6,14,0)^{1-}$ at m/z 2350 (Scheme 1, eqn (1)); second iodide (I^-) loss product $(6,13,0)^{1-}$ at m/z 2223, similar to CID (Scheme 1, eqn (2)); and lastly the radical iodine ($I^\bullet$) loss product $(6,13,0)^{2-\bullet}$ at m/z 1112 (Scheme 1, eqn (3)).

The precursor $(6,14,0)^{2-}$ was first investigated *via* QC calculations with an initial geometry optimization step following the procedure described in the Computational details section. The molecular orbital (MO) energy diagram of $(6,14,0)^{2-}$ is given in Fig. 2 together with the (spin)orbital energy diagram of the primary photo-fragments $(6,14,0)^{1-\bullet}$, $(6,13,0)^{1-}$ and $(6,13,0)^{2-\bullet}$. The frontier MOs are plotted in Fig. S4. The $(6,14,0)^{1-\bullet}$ radical moiety arises from the depopulation of one electron of the highest occupied molecular orbital (HOMO) which is mainly iodide in character (61%). The cluster core and the Mo–I^a bonds are moderately affected by this one-electron oxidation: only a slight elongation of one apex of the Mo_6 octahedra from 2.678 Å to 2.733 Å Mo^{apex}–Mo^{basal} distance, together with a slight shortening of the Mo–I^a distance from 2.881 Å to 2.834 Å. The resulting spin-density is spread over the Mo_6 cluster (Fig. S5), forming an oxidized metal Mo_6 cluster bearing a formal +11 charge, thus $Mo^{1.83+}$. In contrast, the iodine loss ($-I^\bullet$) leads to $(6,13,0)^{2-\bullet}$ where most of the unpaired electron density (0.9) is localized on the iodine-free apical site and the spin density forms a lobe pointing toward the iodine vacancy (Fig. S5). In other words, simulations show that $(6,13,0)^{2-\bullet}$ is a radical species with the radical localized on the lacunar molybdenum, leaving unaffected the oxidation state of the metal Mo_6 cluster. Lastly, the electronic structure of the fragment $(6,13,0)^{1-}$ resulting from iodide loss ($-I^-$) is characterized by the presence of an electron accepting MO (Fig. S5).

From an energetics point of view, the non-adiabatic $I^\bullet \cdots [Mo_6I_{13}]^{2-\bullet}$ iodine-cluster homolytic bond dissociation
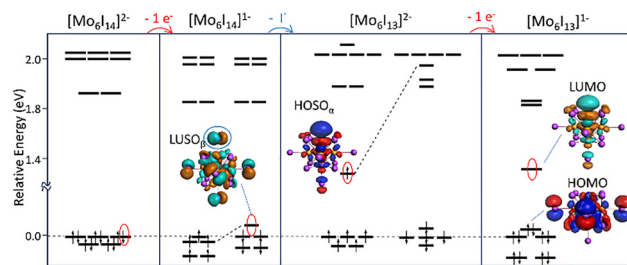

Fig. 2 (Spin) Orbital molecular energy diagram of $[Mo_6I_{14}]^{2-}$, $[Mo_6I_{14}]^{1-\bullet}$, $[Mo_6I_{13}]^{2-\bullet}$, and $[Mo_6I_{13}]^{-}$. For each system the molecular orbital or spin-orbital α ($HOSO_\alpha$) with the same spatial extension and sign as the highest occupied molecular orbitals (HOMO) of the $[Mo_6I_{14}]^{2-}$, were energetically aligned with it. LUMO = lowest unoccupied molecular orbital. LUSO = lowest unoccupied spin-orbital (α or β). Isocontours = ± 0.02 $(e\ Bohr^3)^{\frac{1}{2}}$. The plots of all frontier (spin) orbitals are given in Fig. S4.

energy in the ground state was calculated at 3.547 eV while the $I^- \cdots [Mo_6I_{13}]^{1-}$ heterolytic apical bond dissociation energy was calculated at 0.819 eV. For the sake of comparison, the bromine and bromide bond dissociation energies in $[Mo_6Br_{14}]^{2-}$ were also calculated and are respectively 4.276 eV and 2.523 eV. Thus, the iodinated cluster $[Mo_6I_{14}]^{2-}$ is more susceptible than the brominated cluster $[Mo_6Br_{14}]^{2-}$ (+0.729 eV) to yield the species $(6,13,0)^{2-\bullet}$ by homolytic halogen bond cleavage. This is consistent with the non-observation of $(6,13,0)^{2-\bullet}$ among the LID fragments of $[Mo_6Br_{14}]^{2-}$ (see Fig. S6). However, in both iodinated and brominated cluster simulations, the heterolytic bond cleavage is very significantly favoured with regards to the homolytic cleavage (+2.728 eV and +1.753 eV, respectively). This is consistent with the experimental evidence that the loss of halogenide (I^-/Br^-) represents the major fragmentation feature observed in the gas phase in both CID and LID mass spectra. The calculated ionization potential is +2.755 eV, thus 0.792 eV more accessible than the homolytic cleavage $I^\bullet \cdots [Mo_6I_{13}]^{2-\bullet}$. The QC computed energetics is thus in line with the absence of primary fragments $(6,14,0)^{1-\bullet}$ and $(6,13,0)^{2-\bullet}$ following collisional activation (CID). It suggests that both electron loss (Scheme 1, eqn (1)) and iodine loss (Scheme 1, eqn (3)) are not thermally accessible from the ground state. In contrast, their observation following laser activation (LID) suggests that both phenomena may arise from processes involving electronic excited states.

Optical spectroscopy of $[Mo_6I_{14}]^{2-}$ and wavelength dependence of the primary fragments

Fig. 3 displays the UV-vis optical spectrum of the precursor $(6,14,0)^{2-}$ measured in the gas phase by "action" photo-fragmentation spectroscopy, after mass selection and isolation in the ion trap, overlaid with the simulated spectrum (TDA-DFT calculations, see Computational details). Transitions towards the three first quasi-degenerated excited states (S1, S2 and S3) are calculated at 580 nm in a vacuum and the onset of fragmentation in the visible range is measured accordingly above 560 nm. However, the density of states and transitions increases very significantly around 500 nm which gives rise to two bands respectively at 480 nm and 440 nm in the simulated spectrum convoluted with 20 nm Gaussian profiles (thin black
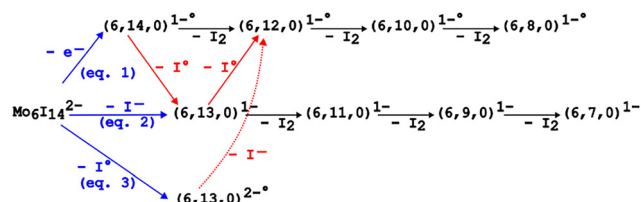
Scheme 1 Three independent photofragments are initially generated by irradiation (blue arrows): loss of an electron (eqn (1)), loss of iodide (I^-, eqn (2)) and loss of iodine ($I^\bullet$, eqn (3)). Clusters depleted in iodine ($(6,12,0)^{1-\bullet}$ to $(6,7,0)^{1-}$) are also observed and may arise as secondary fragments from further losses of I_2 (black arrows) or $I^\bullet$ (red arrows, attested by CID, see Fig. S1 and S2). Loss of I^- is also observed in CID of $(6,13,0)^{2-\bullet}$ (red dotted arrow, see Fig. S3).
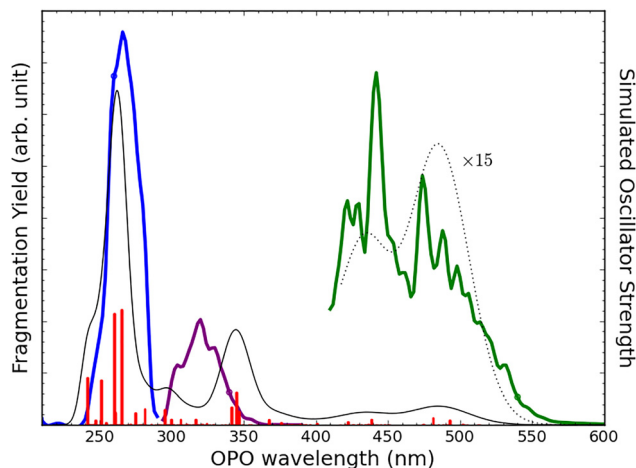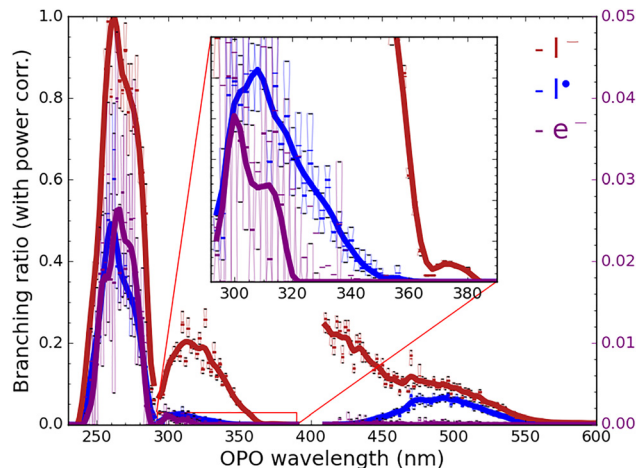
Fig. 3 Optical action (fragmentation) spectrum of $[Mo_6I_{14}]^{2-}$ in the UV-visible range. The photo-fragmentation was recorded independently for three regions: <290 nm (blue), [290–390] nm (purple) and >410 nm (green). Laser irradiance and alignment conditions vary between regions so that their absolute intensities should not be compared. Thus, experimental data was scaled to ease the comparison with the simulated spectrum. Data were recorded with a 2 nm pitch. Circles on the experimental curves represent the position of the laser alignment for each spectral range. The simulated spectrum (thin black line) is calculated from 0.12 eV Gaussian convolution of the oscillator strength for each transition (red bars). A factor $\times 15$ is applied to simulated data in the visible range (dotted line).

Fig. 4 Distribution of the three primary fragments relative intensities as a function of the wavelength. Boxplots represent the 1st and 3rd quartiles of the branching ratios corrected for the laser power profile for the loss of I^- (red) and loss of $I^\bullet$ (blue) on the left axis; and for the e^- loss (purple) on the right axis. Thick lines are smoothed medians to guide the eye.

dotted line in Fig. 3). The experimental spectrum accordingly presents two large, partially unresolved fragmentation bands in the visible range with maxima between 420–440 nm and 470–500 nm. In the UV range, one large band appears between 310 and 350 nm, which corresponds to a 20 nm blue shift with regards to the calculated UV band at 350 nm. Lower in the UV (higher photon energies), one major feature appears on the photo-fragmentation spectrum with a maximum around 270 nm, which matches the major feature from simulations. Overall, the good agreement between experiments and theory enables the use of simulations for a more in-depth interpretation of the fragmentation behaviour.

The specific wavelength dependence of the primary photo-fragments is examined in Fig. 4 and allows several observations. First, the major feature is the clear predominance of the iodide loss over all other primary fragments. This fragment is the only one observed by collisional heating (CID), which retrospectively denotes for LID the importance of internal conversion as a relaxation path from the excited state towards the ground state. It indicates that a large part of the fragmentation might arise from sequential multiple photons' absorption cycle and fragmentation in the ground state.[38]

The second observation is that among the two bands in the visible region, the loss of iodine is only observed in the red-most band at 470–500 nm. Interestingly, natural transition orbital[39] (NTO) analysis of the most intense calculated transitions allows interpreting this asymmetry in terms of the nature of the excited states (see Fig. 5). The strongest transitions in the red-most band correspond to the excited states S_{29} at 495 nm (with oscillator strength $f = 0.023$) and S_{50} at 484 nm (with $f = 0.020$). The NTO

analysis shows that only 20% of S_{29} is described by a transition from the Mo–I^a Sigma bonds to non-bonding NTOs, which corresponds to a partial weakening of the metal–ligand bond. On the other hand, S_{50} hardly affects the metal–ligand bonds but involves a major (72%) character of iodine electron density transfer from apical to inner sites. Thus, transition to S_{50} can be described as the oxidation of the apical iodines (with strong ionic character in the ground state compared to Mo–X^i bonds with strong covalent character) which is susceptible to give rise to radical iodine loss, as observed experimentally. Interestingly, the strongest transition in the second band around 440 nm corresponds to excited state S_{92} at 439 nm (oscillator strength, $f = 0.017$). NTO analysis of S_{92} shows a major loss of Mo–I^a π/d-antibonding character partially transferred to Mo–I^a σ/d-antibonding levels, but globally the iodine electron density is maintained. This band is thus, as observed experimentally, more susceptible to evolve through prompt dissociation of iodide (I^-) compared to the bands at lower energy examined previously.

The third observation is that electron detachment leading to $(6,14,0)^{1-\bullet}$ is only observed below 320 nm. This is consistent with prior photoelectron spectroscopy experiments by Warneke et al.[21] who reported adiabatic/vertical electron binding energies of 2.2–2.4 eV (560–515 nm) and repulsive Coulomb barriers of 1.6 eV, leading to a minimum of 3.8–4.0 eV (i.e. one photon of 310–340 nm) required to efficiently photo-detach an electron from $(6,14,0)^{2-}$. Since the Mo_6 clusters are rigid and no major rearrangement occurs in the ionized state (hence the very small differences between adiabatic/vertical ionization energies), no major effect of the solution phase environment is expected on their ionization properties. As a result, the photo-detached species (either the iodinated but even more the brominated species which are not even formed in the gas phase) are unlikely to be formed in solutions irradiated by visible light and are, thus, unlikely to explain the reactivity observed in solution.[3] Thus, it is likely that this photo-oxidized species is
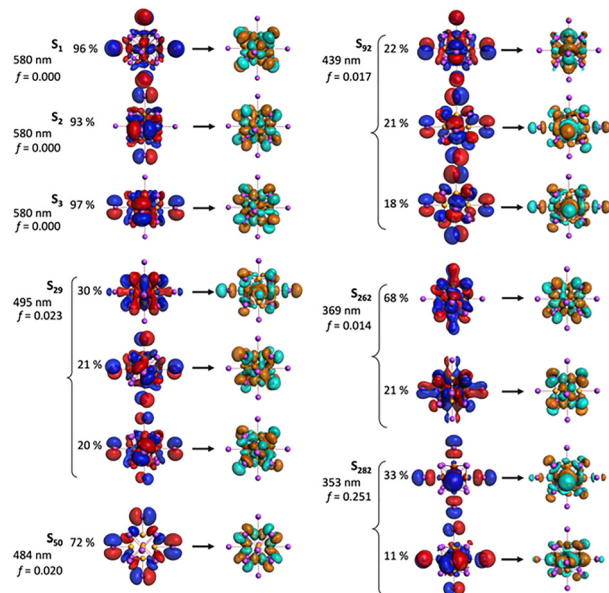
This journal is © the Owner Societies 2025

Phys. Chem. Chem. Phys., 2025, **27**, 23166–23178 | **23169**

Fig. 5 Electron/hole natural transition orbital representations of the three lowest degenerated excited states, and of the excited states of $[Mo_6I_{14}]^{2-}$ with oscillator strengths $f > 0.007$ (only one of the three degenerated states is represented in each case).
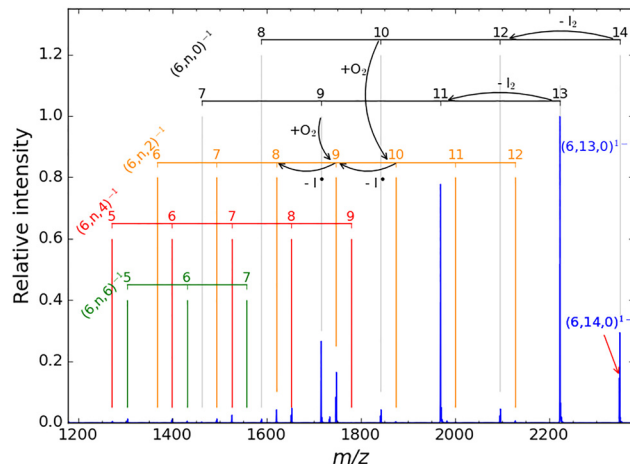

Fig. 6 Photo-fragmentation spectrum (LID) at 260 nm of a single isotopic peak (m/z 1175.2) of the precursor ion $(6,14,0)^{2-}$ denoted by a star (zoomed in LID spectrum shown in Fig. 1). The focus is made on secondary fragment ion series: $(6,n,0)^{1-}$ iodine-depleted ions (grouped in I_2 loss series), and $(6,n,2k)^{1-}$ reaction products with one, two and three O_2 molecules. Example of $-I_2/+O_2/-I^\bullet$ inter-series connectivity is shown with curved black arrows. See SI Table S1 for details of assignments.

not involved as a reactive intermediate in the photo-catalytic cycle. However, since the reported electron binding energy is relatively low, within reach of a photon in the visible range, it is very likely that $(6,14,0)^{2-}$ behaves as a visible-light activated photo-reducer in the excited state. Alternatively, since both iodide loss $(-I^-)$ and iodine loss $(-I^\bullet)$ are observed in the visible range, they might play a role as photo-prepared reactive intermediates and their respective reactivity should be investigated.

The last observation is that below 300 nm the electron, iodide and radical iodine losses present similar band shapes, pointing towards a low spectral selectivity in the UV. However, even if band shapes are similar, iodide loss dominates by a factor of 2 over the photo-specific radical iodine loss, which in turn dominates the electron photo-detachment by a factor of 20.

In summary, a photo-reducer excited state Mo_6 cluster might be formed with low-energy photons (≥ 560 nm) with a reduced propensity for fragmentation. The radical $(6,13,0)^{2-\bullet}$ is optimally formed (relative to other fragments) around 500 nm. The oxidized species $(6,14,0)^{1-\bullet}$ is only formed below 320 nm and is never a major fragment. Overall, the path with I^- loss systematically dominates other fragmentation paths.

Secondary fragments $(6,n,0)^{1-}$

In addition to the three primary photo-fragment ions discussed above, several ion series are observed in the LID mass spectrum (see Fig. 6 and Scheme 1). A full description is given in SI Complements S2 with complete QC and MS^n experiments supporting assignments and discussions on the dissociation mechanisms. In brief, the first series corresponds to iodine depleted cluster complexes from $(6,12,0)^{1-}$ to $(6,7,0)^{1-}$. They may arise as secondary fragments from photo-specific sequential losses of I_2 (Scheme 1, black arrows) or from consecutive $I^\bullet$

losses (Scheme 1, red arrows). In general, and although QC geometry optimization indicates that all $I^\bullet$ loss reactions are largely endergonic (around 3 eV, see Fig. 7), iodine loss would be consistent with prior mass spectrometry results by Warneke *et al.*[22] which revealed that upon collisional activation and after the initial loss of iodide I^-, further losses of halogen radicals represent the main fragmentation channels.

In any case, whether it results from I_2 or from $I^\bullet$ losses, the formation of such secondary fragments is energy demanding and requires excess energy in the primary fragments.

Interestingly, Warneke and coworkers have shown with ion mobility and computational simulations that the octahedral Mo_6 structure remains largely unchanged in the iodine-depleted Mo_6 complexes.[22] This is consistent with prior ion mobility mass spectrometry results in our group which showed that the Mo_6 cluster size and shape are retained irrespective of the chemical nature of the ligands (halogenides or hydroxides),[40] which advocates for a very robust Mo_6 octahedral cluster structure. It is also what we calculate for the series $(6,n,0)^{1-}$ for n ranging from 14 to 5. It should nevertheless be emphasized that the symmetry of the Mo_6 core is importantly decreased. Indeed, in order to compensate for the electronic depletion due to the iodine departure, the metal–metal bonds involving the more I-depleted Mo atoms are importantly shortened: down to 2.391 Å in $(6,5,0)^{1-}$, compared to 2.678 Å in the parent $(6,14,0)^{2-}$ cluster. The shorter Mo–Mo distance in I-depleted sites is in the order of magnitude of reported triple Mo–Mo bonds (while close to bond order 1 in the parent cluster).[41]

Reactivity of the photofragments with O_2

Another series of ions observed on the LID mass spectra corresponds to the addition of one or multiple O_2 on the complexes. While oxygenation products are absent for both

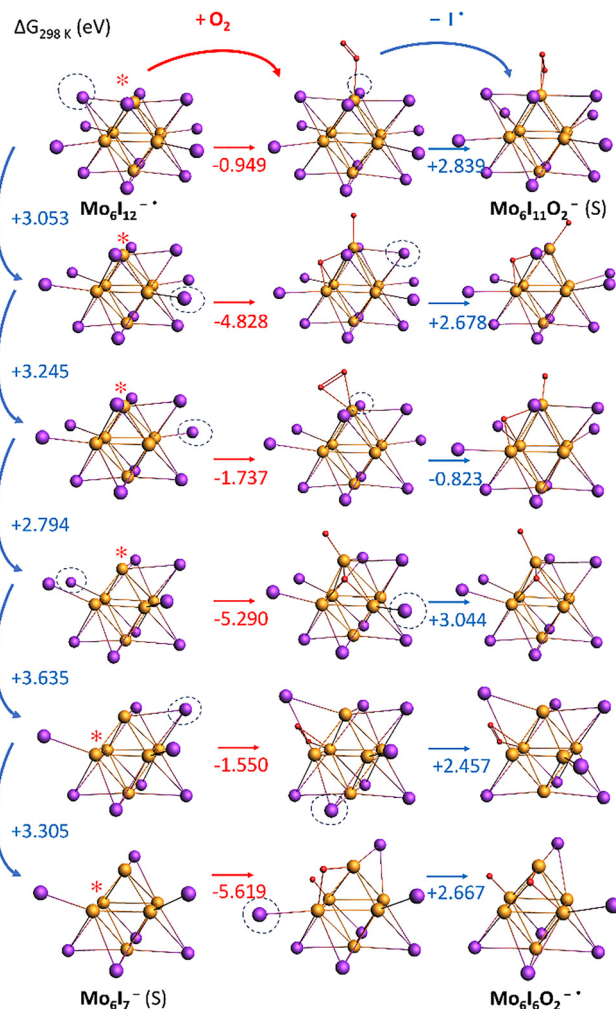**23170** | *Phys. Chem. Chem. Phys.*, 2025, **27**, 23166–23178

This journal is © the Owner Societies 2025

Fig. 7 Difference of Gibbs free energy at 298 K of sequential iodine loss and O_2 addition reactions starting from the most stable isomer of $(6,12,0)^{1-}$. These energies (in eV) correspond to the reaction leading to the most stable possible isomer (S = singlet state; more details in the SI). The red star indicates the Mo centre close to which the O_2 molecule was positioned to generate the $(6,n,2)^{1-}$ initial geometry. The dotted circles show which iodine atom was removed to yield the most stable $(6,n-1,0)^{1-}$ and $(6,n-1,2)^{1-}$ isomers. See SI Table S4 for all reaction energy changes.

$(6,14,0)^{1-\bullet}$ and $(6,13,0)^{1-}$ even at long reaction times (300 ms in Fig. S7 and S8), they are observed for $(6,12,0)^{1-\bullet}$ and further iodine-depleted complexes. Noteworthy, there are only trace levels of O_2 in the ion trap. However, the 10 Hz laser repetition rate together with the asynchronous mass spectrometer behaviour enforces on average a significant delay between the irradiation of selected precursors and the detection of the fragment ions. In our single laser pulse experiments, photo-product ions experience an average 60 ms reaction time post-irradiation, which is enough for several collisions to occur between ions and neutrals, even at trace levels below 1‰ in the background gas at the trap pressure (5 mTorr (ref. 42)). While the formation of H_2O adducts is not common but not atypical in mass spectrometry (since most of the ESI experiments use at least partially aqueous solvent mixtures and the addition of water often corresponds to an early sample

solvation stage with stabilizing H-bonds possible with most organic samples), the addition of O_2 is on the contrary very unusual under ion trap conditions where very low oxygen trace levels are expected. Thus, the appearance of such O_2 adducts (see the orange series in Fig. 6 and peak list in Table S1) reveals a specific affinity between O_2 and the Mo_6 cluster-based complexes. Further series of ions displaying up to 3 O_2 additions were observed (red and green series in Fig. 6).

Globally, the greater the depletion in iodine ligands, the more oxygenated the clusters become. Fig. 8 shows that the single O_2 addition onset appears after the loss of at least 2 iodine atoms from the Mo_6 complex (blue trace), but becomes systematic and the major cluster components after 4 iodine losses. Similar observations and onset of reactivity with O_2 were also reported by Warneke and coworkers[22] under similar ion trap conditions.

Lastly, the third primary photo-product ion $(6,13,0)^{2-\bullet}$ was also observed to react with O_2, with $(6,13,2)^{2-\bullet}$ becoming the major product ion after 250 ms reaction time (Fig. S9). Although both $(6,13,0)^{2-\bullet}$ and $(6,13,0)^{1-}$ display one non-coordinated site, no sign of reactivity with O_2 is observed for the singly charged $(6,13,0)^{1-}$ (see Fig. 8 and Fig. S10). This is consistent with computations which reveal that the O_2 addition to $(6,13,0)^{1-}$ is not significantly favoured: only very slightly exergonic towards the most stable geometry and spin state of $(6,13,2)^{1-}$ (triplet state, $\Delta G_{298K} = -0.023$ eV) and even weakly endergonic towards its most stable singlet state ($\Delta G_{298K} = 0.082$ eV). Interestingly, our experimental results reveal that the O_2 affinity of the dianion $(6,13,0)^{2-\bullet}$ is comparable to that of $(6,12,0)^{1-\bullet}$, which has two vacant sites with radical character: ~10% O_2 adduct formation under the same experimental conditions, Fig. 9. This is also consistent with QC calculations of ΔG_{298K} for the O_2 addition reactions which are of the same
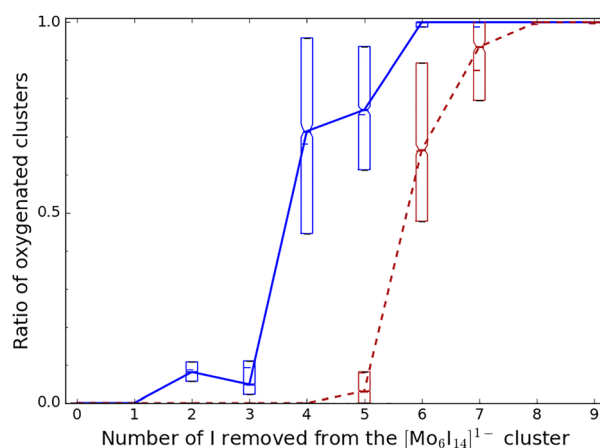

Fig. 8 Evolution, as a function of the number of I removed from the precursor, of the complex oxygenation ratio (continuous line) calculated as the sum of all $(6,k,2n)^{1-}$ ion intensities ($n \geq 1$) normalized by the sum of all $(6,k,2n)^{1-}$ ion intensities ($n \geq 0$). The dashed red line corresponds to the ratio of multiple oxygenation $(6,k,2n+2)^{1-}$ ($n \geq 1$) normalized by $(6,k,2n)^{1-}$ ($n \geq 0$). Data are averaged from the 4 experimental fragmentation ranges in the UV and visible ranges.
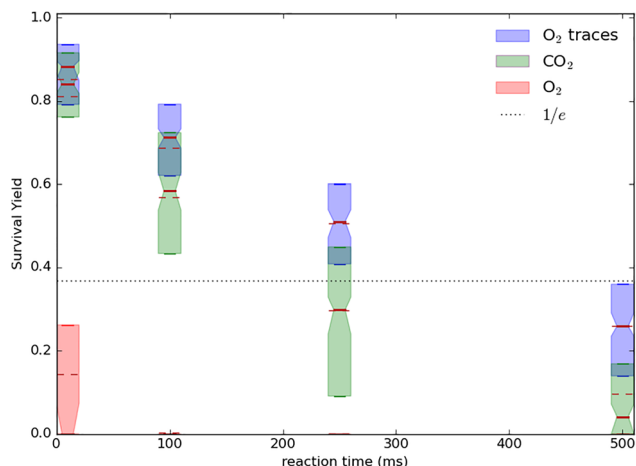
This journal is © the Owner Societies 2025

Phys. Chem. Chem. Phys., 2025, **27**, 23166–23178 | **23171**

Fig. 9 Evolution of the precursor ion $[Mo_6I_{13}]^{2-\bullet}$ survival yield after variable reaction times in the ion trap filled with various background gas compositions: He with unavoidable traces of O_2, 0.5% O_2 seeded in helium, 0.5% CO_2 seeded in helium. Boxplot boundaries represent the first and 3 quartiles; thick continuous and thin dashed red lines show the respective positions of the median and the mean for each reaction time dataset. Notches give impressions of the uncertainty windows estimated *via* a bootstrap approach. The dotted line corresponds to the 1/e level relevant for mono-exponential decays.

order of magnitude, respectively -0.949 eV and -1.221 eV for $(6,12,0)^{1-\bullet}$ and $(6,13,0)^{2-\bullet}$.

Interestingly, the addition of a second O_2 on the complexes is shifted by 2 iodine losses in Fig. 8 (red curve), which suggests that, beyond the onset, binding of O_2 may involve 2 coordination sites. The O_2 coordination modes on the various $(6,n,0)^{1-}$ parents and their relative energetics were examined closely by QC calculations. The $(6,n-1,0)^{1-}$ parent isomers considered in the present work ($n = 13-7$) were generated by sequential single $I^\bullet$ loss of the most stable $(6,n,0)^{1-}$ isomer starting from $(6,13,0)^{1-}$, considering all apical and inner positions. The reactivity of these $(6,n,0)^{1-}$ ions with O_2 was evaluated for all possible attack positions of the O_2 molecule identified on the basis of the spatial extension of the lowest unoccupied (spin)orbitals (LUMOs/LUSOs) and of the spin density (if applicable).

Warneke and collaborators reported QC calculations on the reaction of O_2 with $(6,n,0)^{1-}$ for $n = 12$ and the subsequent $I^\bullet$ loss leading to $(6,11,2)^{1-}$.[22] Our calculations on these specific systems are in full agreement with their results which show that O_2 binds one of the opposite vacant apical sites in η^1 coordination mode (*via* one oxygen atom) in the most stable $(6,12,2)^{1-}$ isomer. In the present work, we extend the study $(6,n,0)^{1-}$ with $n = 11-7$, testing all active Mo coordination sites. The geometry optimizations reveal that many O_2 coordination modes involving one or multiple Mo binding sites exist, leading to inner, face-capping or edge bridging modes involving one or the two oxygen atoms. Interestingly, the most stable $(6,11,0)^{1-}$ isomer possesses one vacant apical site and one adjacent inner vacant site. The most stable optimized $(6,11,2)^{1-}$ isomer has a structure in which O_2 is fully dissociated with one of the oxygen atoms in an apical position and the second oxygen atom in a μ_3 bridging, inner position (Fig. 7). The optimized $(6,9,0)^{1-}$

structure which has 4 free apical sites and one inner site available for coordination gives rise to the same O_2 full dissociation. For $(6,10,0)^{1-}$ and $(6,8,0)^{1-}$, the most stable structures possess respectively 3 and 5 vacant apical sites and one vacant inner site and the most stable O_2 adducts display η^2O_2 coordination to an apical position. Lastly, the optimized $(6,7,0)^{1-}$ contains 5 vacant apical sites and 2 vacant inner sites and the optimized O_2 adduct yields full O_2 dissociation with one O in the apical position and the other oxygen atom in the μ_2 edge-bridging position. Note that the optimized O_2 adduct geometries, for all $(6,n,2)^{1-}$ species, result from the geometry optimization of systems including an O_2 molecule positioned close to reactive Mo sites on the $(6,n,0)^{1-}$ isomers.

From the energetics point of view, QC simulations show that the coordination of O_2 is systematically exergonic for all clusters with $n \leq 12$, irrespective of the O_2 coordination mode on $(6,n,0)^{1-}$ (see energies of all calculated systems in Table S3 and reaction energy changes in Table S4). However, the extent of exergonicity strongly depends on the coordination mode of O_2 on the cluster. Typically, η^1O_2 releases less than 1 eV while η^2O_2 releases 1.5–1.7 eV and O_2 dissociation releases considerably more energy: 4.8 to 5.6 eV. Similarly, QC calculations show that the magnetic character (non-zero spin value) of the parent iodine cluster is not a prerequisite to the O_2 addition. However, the spin state of the most stable parent cluster seems to affect the coordination mode of O_2, in particular its dissociation fate, and therefore the exergonicity of the reaction between the $(6,n,0)^{1-}$ clusters and O_2.

Interestingly, as soon as O_2 is coordinated more strongly than η^1 (*i.e.* for $(6,n,2)^{1-}$ with $n \leq 11$), the exergonicity of O_2 additions may be large enough to induce further fragmentation, especially in a dilute gas phase environment where internal energy cannot diffuse away *via* collisions with the solvent. In particular, the large exergonicity may compensate for the global endergonicity of $I^\bullet$ losses and yield another $I^\bullet$ loss (see Fig. 7). Thus, O_2 binding $(6,11,0)^{1-}$ may favorably yield the $(6,10,2)^{1-}$ species by $I^\bullet$ loss ($2.678-4.828 = -2.150$ eV) whereas O_2 binding $(6,12,0)^{1-}$ may not decay into $(6,11,2)^{1-}$ ($2.839-0.949 = +1.890$ eV). These QC calculations are consistent with experiments in both the current work and that of Warneke *et al.*[22] where the O_2 addition onto $(6,n,0)^{1-}$ is generally followed by an $I^\bullet$ loss for $n \leq 11$. However, it is interesting to observe that the most stable structure yielded after O_2 addition followed by $I^\bullet$ loss may be different from the structure resulting from $I^\bullet$ loss followed by O_2 addition: the coordination of O_2 affects the preferential iodine departing site, which limits the O_2 coordination rearrangement in the final structure (see for instance $(6,11,2)^{1-}$ coming from $(6,11,0)^{1-}$ or $(6,12,2)^{1-}$ in Fig. 7).

According to the calculations, the onset of reaction with O_2 in Fig. 8 can be associated with the radical character of available binding sites on the cluster complex where O_2 may bind as $\mu_0\eta^1$. This property is applicable for $(6,n,0)^{1-}$ species with $n = 12, 10, 8$ (which are, according to simulations, doublets with strong radical character) as well as for $(6,13,0)^{2-\bullet}$. This is consistent with the increased reaction rate of O_2 with open-

23172 | *Phys. Chem. Chem. Phys.*, 2025, **27**, 23166–23178

This journal is © the Owner Societies 2025

shell transition metal clusters described in the literature (see the very complete review by Fielecke[11]), and has been explained by their lower electron binding energies correlated with a facilitated electron transfer towards O_2 to yield the superoxo $\eta^1 O_2$ structure. Then, the sudden step in oxidation ratios measured after 4 iodine losses likely results from the increased O_2 affinity for the cluster with increased binding strengths permitted by the appearance of neighboring free sites that allow both $\eta^2 O_2$ binding (peroxo structures have also been described by Fielecke[11]) but also, more importantly, O_2 dissociation that yields oxo structures (see Fig. 7). In addition to this increased affinity, the large exergonicity associated with O_2 dissociation is responsible for the $(6,11,2)^{1-}$ oxygenated cluster dissociation into $(6,10,2)^{1-}$, which explains the unexpectedly low and high apparent oxidation ratios measured for $n = 11$ and 10 in Fig. 8. More generally, the exergonic character of the $\eta^2 O_2$ binding, and even more markedly the exergonicity of the O_2 dissociation on the cluster, may be at the foundation of the extended dehalogenation and advanced oxygenation of the Mo_6 cluster complexes as observed experimentally in the present work (see Fig. 10 bottom panel). The structure and energetics of the fully oxygenated species extend beyond the scope of the present paper and will be described in more detail in a future communication.

Interestingly, despite the large exergonic character of $\eta^2 O_2$ or O_2 dissociative binding, no fragmentation of the cluster core is observed experimentally. Actually, cluster core fragmentation was only observed after reaction of the dianionic $(6,13,0)^{2-\bullet}$ with O_2 (Fig. S3 with CID and S9 without CID but 250 ms IMR with O_2 traces). In both cases, aside from a major peak corresponding to $(6,13,2)^{2-\bullet}$ and the associated iodine loss product $(6,12,2)^{2-}$, two major fragment ions are detected with complementary masses summing up to the oxygenated precursor ion and with isotopic patterns typical for respectively $[MoI_2O_2]^-$ and $[Mo_5I_{11}]^-$ (especially visible in Fig. S9). This points towards the Mo_6 core fragmentation from the $(6,13,2)^{2-\bullet}$ species, i.e. after addition of O_2 on the precursor radical dianion. Additional cluster core fragments are observed at m/z 1652 and 1525 (Fig. S9 and S11) and tentatively assigned to $(4,10,0)^{1-}$ and $(4,9,0)^{1-}$, respectively. As a confirmation, longer reaction times (250 ms, Fig. S9) yield higher $[MoI_2O_2]^-$ peak intensity and further core fragmentation than shorter reaction times (100 ms, Fig. S11 top panels). Also, when the trapping atmosphere is seeded with 0.5% O_2 (Fig. S11 middle panels), all reactions immediately shift towards oxygenated products (in particular, species $(6,13,2)^{2-\bullet}$ becomes the most abundant dianion within less than 100 ms) and all ensuing secondary products massively increase, in particular the Mo_6 core degradation paths. Interestingly, MoI_2O_2 has been reported as neutral in the gas phase,[43] with the Mo^{VI} oxidation state. The observed species $[MoI_2O_2]^-$ was never reported individually:
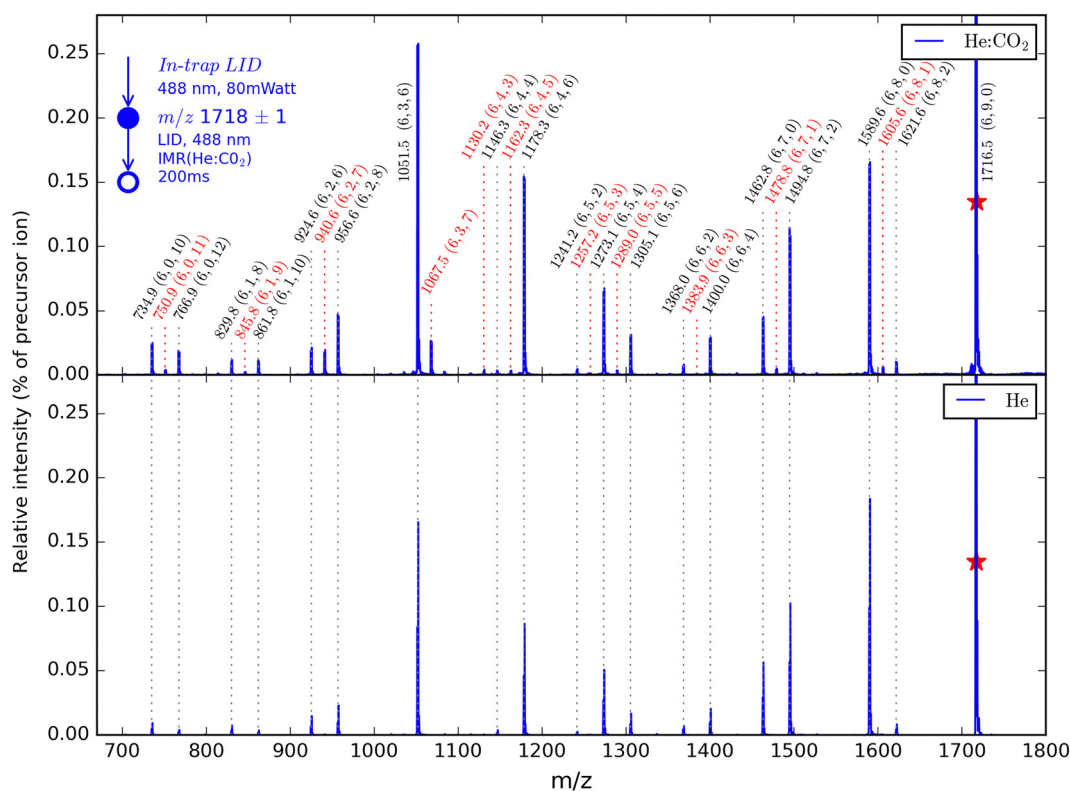
Fig. 10 Ion–molecule reactions under irradiation (photo-IMR-MS^2) spectra of precursor species $(6,9,0)^{1-}$. No collisional energy is applied but precursors are irradiated with a CW laser at 488 nm (80 mW) during the whole experiment, from the ion accumulation/injection time, through the 200 ms reaction time with the background gas and up to ion detection. Background gas composition: helium with O_2 traces (bottom) and He seeded with 0.5% CO_2 (top). $(6,n,2k)^{1-}$ adducts formed by reaction with O_2 are marked in black while $(6,n,2k + 1)^{1-}$ adducts specifically formed in the presence of CO_2 are marked in red. See SI Table S2 for details on assignments.

This journal is © the Owner Societies 2025

Phys. Chem. Chem. Phys., 2025, **27**, 23166–23178 | **23173**

oxidation state Mo^V is well known but predominantly exists under the form of metal dimers sharing *e.g.* an oxo-bridge.[44,45] The Mo^V is nevertheless a stable oxidation state, thus fragment $[MoI_2O_2]^-$ is not unexpected. However, the $[MoI_2O_2]^-$ fragment is only formed from the di-anionic, oxygenated $(6,13,2)^{2-\bullet}$. The cluster complex fragmentation was never observed previously for the iodinated Mo_6X_{14} mono- or di-anions, and was observed only for higher collision energies (between 80 and 150 V) for the chlorinated clusters.[22] These elements point towards the specific instability of the Mo_6 core in $(6,13,2)^{2-\bullet}$. This is consistent with QC calculations which show that the coordination of O_2 leads to the destabilization by ~ 0.2 eV of the HOMO in $(6,13,2)^{2\bullet}$. In addition, the analysis of the simulated geometry of $(6,13,2)^{2-\bullet}$ (see Fig. S12) shows that O_2 binds at the apical free site in η^2 mode while an inner face-capping iodine decoordinates from the Mo which binds O_2 (Mo^{O_2}) to become edge bridging on the opposite 2 Mo of its original face. This is accompanied by the Mo^{O_2}–Mo bond weakening (elongation up to 2.828 Å) together with the elongation of the Mo–I distances.

Reactivity of the photofragments with CO_2

Primary photo-fragments and comparison between O_2 and CO_2. In view of the photo-catalytic character of the Mo_6 cluster complexes, the reactivity of the photo-specific fragments was investigated with CO_2. At 0.5% seeding percentage, the collision rate of CO_2 with the precursor dianions/monoanions is calculated as $\sim 910/455$ collisions per second in the HPT (see the Methods section and more details in the SI, section Complements S1). Neither $(6,14,0)^{1-\bullet}$ nor $(6,13,0)^{1-}$ displays any sign of reaction. In the case of $(6,13,0)^{2-\bullet}$, all three previously identified reaction paths are maintained: first, formation of the oxidized $(6,13,2)^{2-\bullet}$ species, and subsequently loss of $I^\bullet/I^-$ or Mo_6 core dissociation (see Fig. S11, bottom panels). The relative intensities of these reaction products are nevertheless much lower than in $He:O_2$. For instance, after 100 ms reaction time, the precursor ion $(6,13,0)^{2-\bullet}$ is still the major species detected in $He:CO_2$ ($\sim 60\%$ of the total ion signal on the full m/z range [305–2500]) while it has nearly completely reacted in $He:O_2$ ($\sim 0.4\%$ of the signal). This observation confirms that these paths are bound to the initial reaction with O_2 (the concentration of which falls back to trace levels in $He:CO_2$). The absence of any specific and new reaction product ion in the mass spectrum after the introduction of CO_2 discards the possibility of a direct chemical route between the precursor and CO_2. Since CO_2 is not itself a radical, the radical character $(6,13,0)^{2-\bullet}$ must be set aside and it can only be concluded that it is not a potent enough reducing agent to directly reduce the very stable CO_2.

However, unexpectedly, the O_2-related fragments' intensities rise a little compared to unseeded helium, which is reflected by a significantly lower survival yield in CO_2 than helium as reaction time increases. Fig. 9 displays the precursor relative intensity as a function of trapping time in helium with traces of O_2 (blue) *vs.* 0.5% CO_2 (green) or 0.5% O_2 (red). Under the rough but reasonable approximation of a first-order kinetics reaction of the precursor with O_2 (maintained at a constant

concentration in the ion trap), the precursor survival yield ought to be modelled with a mono-exponential decay function. Thus, the reaction time constant can be approximated by the reaction time at which the precursor level is down to $1/e$ (Fig. 9 dotted line). In terms of reaction rate, the estimations evolve from 2.5 s^{-1} (400 ms) to 5 s^{-1} (200 ms) from unseeded helium with traces of O_2 to $He:CO_2$. Thus, the precursor disappears nearly twice as fast with 0.5% CO_2 than with only O_2 traces. This enhanced apparent reactivity of the precursor under CO_2 atmosphere, although with exactly identical fragments as with O_2, likely corresponds to a mere collisional activation effect stemming from the high instability of the precursor ion (very small activation energy required to induce reactions, see the above section, "Secondary fragments $(6,n,0)^{1-}$") combined with the frequent collisions (910 s^{-1}) and higher collisional energy between the precursor ions and CO_2 (1 order of magnitude higher in reduced mass compared with helium). This combination is likely to mechanically increase the internal temperature of the precursor ions and result in higher reaction rates.

Remarkably, the reaction rate in 0.5% O_2 can be estimated to be > 200 s^{-1} (< 5 ms), *i.e.* ≥ 80 times faster than in pure helium, with only traces of O_2. Considering a constant reaction rate per collision, the trace level of O_2 in the ion trap with unseeded helium can thus be estimated to be less than 0.5%/80, *i.e.* $\sim 0.005\%$. Since the collision rate between $(6,13,0)^{2-\bullet}$ and O_2 in $He:O_2$ is ~ 840 s^{-1}, the reaction probability per collision with O_2 can be calculated and its lower boundary amounts to 0.24, which is considerable (1 of 4 collisions at least is reactive) and definitely points at O_2 additions as a major limitation to the radical photofragment $(6,13,0)^{2-\bullet}$ lifetime.

Case of the reactivity of highly dehalogenated cluster complexes. Beyond the case of the primary photofragments, the reactivity of under-coordinated Mo_6 cluster-based complexes was also assessed. First, the major observation is that throughout experiments with CO_2, the major ions are identical to what is observed in helium with traces of O_2: $(6,n,2k)^{1-}$ fragments with variable numbers of halogen and dioxygen adducts (Fig. S13 and S14 top). In other words, no major effect is observed due to the presence of CO_2 in the trapping gas. However, two significant observations are made among lower intensity peaks: first, several peaks are detected with unusually large width and asymmetrical shape and, second, several ions are detected with an odd number of oxygen atoms. Both observations, detailed below, are specific to the presence of CO_2.

It is striking that in the presence of CO_2, no CO_2 adduct is apparently formed with cluster complexes displaying multiple binding sites available. However, several peaks are detected with unusually large width and asymmetrical shape at ~ 42 Th above $(6,n,k)^{1-}$ species. For instance, in the CID spectrum of $(6,5,6)^{1-}$ (Fig. S14), such deformed peaks are detected at m/z 999.8 and 1110.1, 42 Th above ions $(6,3,7)^{1-}$ and $(6,2,8)^{1-}$. The width and shape of these peaks recall peak fronting, which has been reported in ion traps, specifically for fragile ions during their ejection towards the detectors.[46,47] During resonant ejection, collisions with the buffer gas may energize the ions: in the case of fragile ions, part of the ions can fragment before ions

23174 | *Phys. Chem. Chem. Phys.*, 2025, **27**, 23166–23178

This journal is © the Owner Societies 2025

reach the detector, which results in deformed peaks with inaccurate mass assignments. By analogy, this suggests that in our experiment the ions detected with such profiles are very fragile/metastable. In addition, the relative amplitude of the fronting and the global mass assignment of these fragile ions depend on the survival of the precursor ions during the ion detection which depends on the scan speed. Yost and co-workers have reported up to 1.09 Th shifts towards low m/z for precursor anions with mass 314 Da.[47] Since the ions detected in the present study are significantly higher in m/z (towards 1000 Th), and the mass resolution of the spectra is significantly higher than in Yost and co-workers' study, it is likely that the scan speed is also significantly slower. Under these conditions, it is expected that the fragile ions' mass shift is higher than that reported previously. Thus, the actual m/z value of the very fragile ions detected in the present study is probably significantly more than 1.09 Th above their measured position. In other words, the hypothesis of short-lived, metastable CO_2 adducts (+44 Da) that do not survive detection is very plausible despite the inaccurate mass difference. Despite the fact that these potential CO_2 adducts have only been observed from oxygenated cluster (Fig. S14) which would suggest the η^1- or η^2-carbonato coordination mode of CO_2 on a metal-oxo site,[11] peak fronting is most probably a sign of weakly physisorbed CO_2 with only little or no electron transfer from the cluster.

Alternatively, CO_2 might bind to the cluster and dissociate rapidly into CO and O and yield, after neutral CO loss, a product anion with an odd-number of oxygen atoms. Such CO_2 activation with CO loss has been observed previously on anionic pure metal clusters,[11] but also on highly reduced transition metal oxide clusters including molybdenum oxide clusters[16] as well as on niobium clusters[17,19,20] and metal carbides.[18] Interestingly, while O_2 addition only yields species with an even number of oxygen atoms, the dissociation of CO_2 might yield species with an odd number of oxygen atoms. In the present study, Mo_6 species with odd numbers of oxygen atoms were observed exclusively in the presence of CO_2 in the trap. Thus, $(6,7,5)^{1-}$ is observed readily after in-source CID of the precursor $(6,14,0)^{2-}$ (Fig. S13) while $(6,2,9)^{1-}$ and $(6,3,7)^{1-}$ are formed after CID of the mass-selected precursor $(6,5,6)^{1-}$ (Fig. S14). These odd numbers of oxygen species are particularly present when ion–molecule reactions with CO_2 are performed under CW irradiation. Fig. 10, top panel, displays an MS^2 spectrum corresponding to reaction for 200 ms of precursor $(6,9,0)^{1-}$ with CO_2 (0.5%) under constant irradiation with a 488 nm CW laser. The following odd numbers of oxygen species are then detected: $(6,0,11)^{1-}$, $(6,1,9)^{1-}$, $(6,2,7)^{1-}$, $(6,3,7)^{1-}$, $(6,4,3)^{1-}$, $(6,4,5)^{1-}$, $(6,5,3)^{1-}$, $(6,5,5)^{1-}$, $(6,6,3)^{1-}$, $(6,7,1)^{1-}$, and $(6,8,1)^{1-}$. Thus, these species seem specifically related to the presence of CO_2 in the ion trap and significantly favoured by irradiation, which is evocative of light induced electron transfer (LIET) from the cluster to CO_2. Remarkably, such LIET seem to be favoured in adducts where no charge transfer occurs in the ground state,[48] which would be the case for transient, weakly bound physisorbed CO_2.

Computational studies were performed considering sequential addition of CO_2 and loss of CO to the most stable isomer of ion $(6,8,0)^{1-}$ observed in Fig. 10. The Gibbs free energies of reaction are given in Fig. 11 together with the geometrical
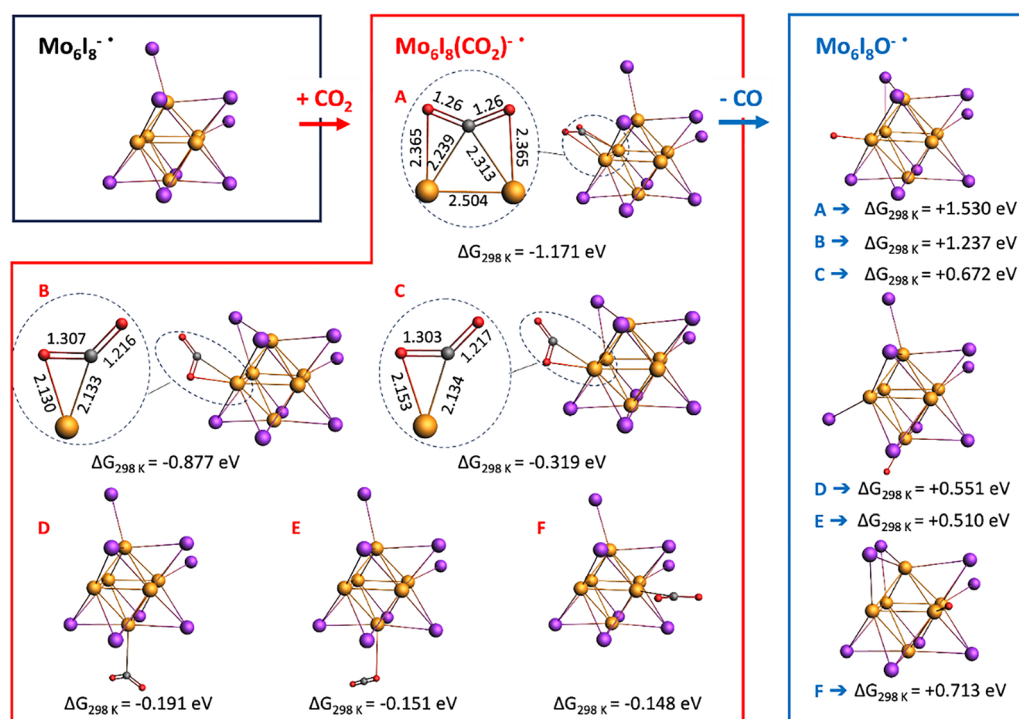

Fig. 11 Difference of Gibbs free energy at 298 K for the sequential addition of CO_2 and loss of CO to the most stable isomer of $(6,8,0)^{1-}$. All possible coordination de-coordination sites are considered. See SI Table S4 for all reaction energy changes.

This journal is © the Owner Societies 2025

Phys. Chem. Chem. Phys., 2025, **27**, 23166–23178 | **23175**

representation of the different isomers. Interestingly, the CO_2 binding is exergonic in all configurations that were found after considering all active binding sites (-0.148 eV $\leq \Delta G^{298K} \geq -1.17$ eV). The CO_2 binding energy remains modest compared to O_2 (3–5 eV, see the prior section) and in any case lower than the Mo–I binding energy, which explains that CO_2 adducts cannot be stabilized by $I^\bullet$ losses as for O_2 adducts and may dissociate rapidly in the gas phase. QC calculations show that CO_2 coordination modes are diverse, similar to what is reported in the literature,[11] with the carbon atoms or the oxygen atom(s) interacting with one or two molybdenum atoms. Simulations on the non-oxygenated $(6,8,0)^{1-\bullet}$ show that CO_2 binding can occur under multiple configurations (Fig. 11), and is associated with various degrees of electron transfer yielding bound CO_2^- and attested by the appearance of an angle in the otherwise linear neutral CO_2: η^1-$\underline{C}O_2$ (isomers D and F), η^1-$O\underline{C}O$ (isomer E), η^2-$\underline{OC}O$ (isomers B and C), and $\mu_2\kappa^3(\eta^2$-$\underline{OC}O, \eta^2$-$O\underline{C}O)$ (isomer A). The most stable adduct, labelled A in Fig. 11, shows a bent configuration of CO_2 where each "CO" branch interacts with a Mo center in η^2 manner. The Gibbs free energies associated with CO loss from these structures are all endergonic with slightly larger absolute energy values than the ΔG^{298K} CO_2 binding. The energy balance for the successive CO_2 binding, dissociation and CO release is endergonic by ~ 0.35 eV for most of the configurations (except F) if the reactions are barrierless. This may explain the added efficiency of odd oxygen species under light irradiation: the absorption of a photon may promote the precursor ion (or the short-lived CO_2 adduct) into a reactive electronically excited state and, more generally, provide the system with the necessary additional energy to enable the dissociation of CO_2.

Conclusions

The photo-activation of the $[Mo_6I_{14}]^{2-}$ cluster ions interestingly yields both the oxidized $[Mo_6I_{14}]^{-\bullet}$ species and the electron-rich $[Mo_6I_{13}]^{2-\bullet}$ radical clusters in addition to $[Mo_6I_{13}]^-$. The latter is also produced by collisional heating (CID). The former two products are both photo-specific since neither is formed by collisional activation. The optical fragmentation spectrum of $[Mo_6I_{14}]^{2-}$ displays features in both the UV and visible ranges, consistent with its QC simulated spectrum. Although the major fragments always include CID-type "thermal" fragments, both photo-specific fragments display remarkable wavelength dependence. The oxidized species $[Mo_6I_{14}]^{-\bullet}$ is only significantly formed below 310–340 nm where photon energies exceed the sum of the repulsive coulombic barriers and electron binding energy. Although this species is only formed in the UV and ion–molecule collisions show no sign of reactivity with CO_2 or O_2, its mere presence is a sign that the cluster possesses strong reducing properties in the electronic excited state. Thus, it is possible that the photo-catalytic reaction takes place when the cluster is in an excited electronic state rather than with a ground state photo-product.

In contrast to $[Mo_6I_{14}]^{-\bullet}$, the radical $[Mo_6I_{13}]^{2-\bullet}$ clusters are formed along the first absorption band in the visible range

~ 500 nm. Since the photo-reduction properties of these Mo_6 clusters have been reported upon irradiation in the visible range, it may seem plausible that $[Mo_6I_{13}]^{2-\bullet}$ is a reactive intermediate in photo-catalytic cycles. However, ion–molecule collisions between CO_2 and the electron-rich $[Mo_6I_{13}]^{2-\bullet}$ showed no sign of reactivity, which discards the possibility for the direct reduction of CO_2. It does not necessarily discard $[Mo_6I_{13}]^{2-\bullet}$ as a reactive intermediate: its electron rich character corresponds to a non-reduced core surrounded by a radical site which could be driving radical reactions with alternative intermediate chemicals. Thus, ion–molecule reactions and QC calculations showed that $[Mo_6I_{13}]^{2-\bullet}$ reactions with O_2 are very efficient and exergonic. However, QC and experiments also show that the oxygenation of $[Mo_6I_{13}]^{2-\bullet}$ was largely responsible for the Mo_6 core destabilization and fragmentation, which could arguably be seen as catalyst poisoning.

Aside from the primary photo-products, many halogen-depleted clusters are observed experimentally via laser irradiation. Halogen depletion yields clusters with stronger metal–metal bonds compared to the original $[Mo_6I_{14}]^{2-}$ species, reinforcing the metallic character of the cluster. These species also react very efficiently with O_2 and QC calculations show that these reactions are all exergonic, with associated ~ 5 eV or more released upon O_2 dissociation. Binding of O_2 becomes quantitative with at least 3 vacant/radical sites, i.e. when apical-to-face-capping scrambling allows for bridging O_2 or dissociative binding configuration of the oxygens on the cluster. Lastly, ion–molecule reactions between these halogen-depleted clusters and CO_2 show, under constant irradiation, proof of CO_2 reduction into CO and O, with the release of CO and formation of the oxidized clusters. QC predicts that these reactions are slightly endergonic and may be favoured in the excited spin states, which could explain the specific role of photon excitation. The release of CO and formation of oxo complexes is in line with similar reactions on small metal clusters and points a priori towards Mo_6 acting as a sacrificial photo-reactant rather than a photocatalyst.

Author contributions

All authors contributed to the conceptualization; experimental investigations were performed by AT, LMA and ROH; computational investigations were performed by NT and KC; data curation was performed by AT, LMA, NT and KC. The manuscript was written through contributions of all authors. All authors have given approval to the final version of the manuscript.

Conflicts of interest

There are no conflicts to declare.

Data availability

Cartesian coordinates for all computed structures are available at: **https://doi.org/10.5281/zenodo.15519713**. MS data are available anytime upon request to LMA.

23176 | *Phys. Chem. Chem. Phys.*, 2025, **27**, 23166–23178

This journal is © the Owner Societies 2025

The data supporting this article have been included as part of the supplementary information (SI). Supplementary information includes details on (1) the collision rate calculations; (2) the secondary fragmentation; (3) the experimental optical spectroscopy method; (4) the COSMO correction. Tables reporting peak list, mass differences and assignments for all MS data shown are included. Tables reporting energies calculated for all species and reactions envisaged are included. Additional figures are included (optical data analysis, CID/LID-MS^2 spectra of various ions, representation of the frontier MOs and spin density for primary species, IMR-MS^2 spectra of various photo-products). See DOI: **https://doi.org/10.1039/d5cp02611c**.

Acknowledgements

Notes and references

1 Z. Luo, A. W. Castleman and S. N. Khanna, Reactivity of Metal Clusters, *Chem. Rev.*, 2016, **116**, 14456–14492.

2 M. Feliz, M. Puche, P. Atienzar, P. Concepción, S. Cordier and Y. Molard, In Situ Generation of Active Molybdenum Octahedral Clusters for Photocatalytic Hydrogen Production from Water, *ChemSusChem*, 2016, **9**, 1963–1971.

3 P. Kumar, S. Kumar, S. Cordier, S. Paofai, R. Boukherroub and S. L. Jain, Photoreduction of CO$_2$ to methanol with hexanuclear molybdenum [Mo$_6$Br$_{14}$]$^{2-}$ cluster units under visible light irradiation, *RSC Adv.*, 2014, **4**, 10420.

4 S. Cordier, F. Grasset, Y. Molard, M. Amela-Cortes, R. Boukherroub, S. Ravaine, M. Mortier, N. Ohashi, N. Saito and H. Haneda, Inorganic Molybdenum Octahedral Nanosized Cluster Units, Versatile Functional Building Block for Nanoarchitectonics, *J. Inorg. Organomet. Polym. Mater.*, 2015, **25**, 189–204.

5 S. Akagi, S. Fujii and N. Kitamura, A study on the redox, spectroscopic, and photophysical characteristics of a series of octahedral hexamolybdenum(II) clusters: [{Mo$_6$X$_8$}Y$_6$]$^{2-}$ (X,Y = Cl, Br, or I), *Dalton Trans.*, 2018, **47**, 1131–1139.

6 P. Kumar, H. P. Mungse, S. Cordier, R. Boukherroub, O. P. Khatri and S. L. Jain, Hexamolybdenum clusters supported on graphene oxide: Visible-light induced photocatalytic reduction of carbon dioxide into methanol, *Carbon*, 2015, **94**, 91–100.

7 A. Barras, M. R. Das, R. R. Devarapalli, M. V. Shelke, S. Cordier, S. Szunerits and R. Boukherroub, One-pot synthesis of gold nanoparticle/molybdenum cluster/graphene oxide nanocomposite and its photocatalytic activity, *Appl. Catal., B*, 2013, **130–131**, 270–276.

8 N. T. K. Nguyen, C. Lebastard, M. Wilmet, N. Dumait, A. Renaud, S. Cordier, N. Ohashi, T. Uchikoshi and F. Grasset, A review on functional nanoarchitectonics nanocomposites based on octahedral metal atom clusters (Nb6, Mo6, Ta6, W6, Re6): inorganic 0D and 2D powders and films, *Sci. Technol. Adv. Mater.*, 2022, **23**, 547–578.

9 D. G. Nocera and H. B. Gray, Electrochemical reduction of molybdenum(II) and tungsten(II) halide cluster ions. Electrogenerated chemiluminescence of tetradecachlorohexamolybdate(2-) ion, *J. Am. Chem. Soc.*, 1984, **106**, 824–825.

10 F. Tureček, UV-vis spectroscopy of gas-phase ions, *Mass Spectrom. Rev.*, 2023, **42**, 206–226.

11 A. Fielicke, Probing the binding and activation of small molecules by gas-phase transition metal clusters via IR spectroscopy, *Chem. Soc. Rev.*, 2023, **52**, 3778–3841.

12 J. Zelenka and J. Roithová, Mechanistic Investigation of Photochemical Reactions by Mass Spectrometry, *ChemBioChem*, 2020, **21**, 2232–2240.

13 P. Armentrout, Reactions And Thermochemistry Of Small Transition Metal Cluster Ions, *Annu. Rev. Phys. Chem.*, 2001, **52**, 423–461.

14 L. G. Dodson, M. C. Thompson and J. M. Weber, Characterization of Intermediate Oxidation States in CO$_2$ Activation, *Annu. Rev. Phys. Chem.*, 2018, **69**, 231–252.

15 H. Schwarz, Metal-mediated activation of carbon dioxide in the gas phase: Mechanistic insight derived from a combined experimental/computational approach, *Coord. Chem. Rev.*, 2017, **334**, 112–123.

16 E. Hossain, D. W. Rothgeb and C. Chick Jarrold, CO$_2$ reduction by group 6 transition metal suboxide cluster anions, *J. Chem. Phys.*, 2010, **133**, 024305.

17 Y.-H. Zhang and J.-B. Ma, Consecutive Reduction of Five Carbon Dioxide Molecules by Gas-Phase Niobium Carbide Cluster Anions Nb$_3$C$_4^-$: Unusual Mechanism for Enhanced Reactivity by the Carbon Ligands, *J. Phys. Chem. A*, 2024, **128**, 2323–2329.

18 X.-Y. He, Y.-Z. Liu, S.-D. Wang, X. Lan, X.-N. Li and S.-G. He, Multiple CO$_2$ reduction mediated by heteronuclear metal carbide cluster anions RhTaC$_2^-$, *Dalton Trans.*, 2022, **51**, 11491–11498.

19 L. Song, A. Eychmueller, R. J. St. Pierre and M. A. El-Sayed, Reaction of carbon dioxide with gaseous niobium and niobium oxide clusters, *J. Phys. Chem.*, 1989, **93**, 2485–2490.

20 H.-Y. Zhou, M. Wang, Y.-Q. Ding and J.-B. Ma, Nb$_2$BN$_2^-$ cluster anions reduce four carbon dioxide molecules: reactivity enhancement by ligands, *Dalton Trans.*, 2020, **49**, 14081–14087.

21 R.-Z. Li, Q. Yuan, Z. Yang, E. Aprà, Z. Li, V. A. Azov, K. Kirakci, J. Warneke and X. Wang, Photoelectron spectroscopy of [Mo$_6$X$_{14}$]$^{2-}$ dianions (X = Cl–I), *J. Chem. Phys.*, 2019, **151**, 194310.

22 P. Su, Z. Warneke, D. Volke, M. F. Espenship, H. Hu, S. Kawa, K. Kirakci, R. Hoffmann, J. Laskin, C. Wiebeler and J. Warneke, Gas Phase Reactivity of [Mo$_6$X$_{14}$]$^{2-}$ Dianions (X = Cl – I), *J. Am. Soc. Mass Spectrom.*, 2023, **34**, 161–170.

This journal is © the Owner Societies 2025

Phys. Chem. Chem. Phys., 2025, **27**, 23166–23178 | **23177**

23 S. Gronert, Mass Spectrometric Studies of Organic Ion/ Molecule Reactions, *Chem. Rev.*, 2001, **101**, 329–360.

24 C. C. Bright, M. B. Prendergast, P. D. Kelly, J. P. Bezzina, S. J. Blanksby, G. da Silva and A. J. Trevitt, Highly efficient gas-phase reactivity of protonated pyridine radicals with propene, *Phys. Chem. Chem. Phys.*, 2017, **19**, 31072–31084.

25 R. A. J. O'Hair, Mass spectrometry based studies of gas phase metal catalyzed reactions, *Int. J. Mass Spectrom.*, 2015, **377**, 121–129.

26 K. Kirakci, S. Cordier and C. Perrin, Synthesis and Characterization of $Cs_2Mo_6X_{14}$ (X = Br or I) Hexamolybdenum Cluster Halides: Efficient Mo_6 Cluster Precursors for Solution Chemistry Syntheses, *Z. Anorg. Allg. Chem.*, 2005, **631**, 411–416.

27 L. L. Lopez, P. R. Tiller, M. W. Senko and J. C. Schwartz, Automated strategies for obtaining standardized collisionally induced dissociation spectra on a benchtop ion trap mass spectrometer, *Rapid Commun. Mass Spectrom.*, 1999, **13**, 663–668.

28 R. Rüger, M. Franchini, T. Trnka, A. Yakovlev, E. van Lenthe, P. Philipsen, T. van Vuren, B. Klumpers and T. Soini, AMS 2022.1, SCM, Theoretical Chemistry, Vrije Universiteit, Amsterdam, The Netherlands, 2022, https://www.scm.com.

29 G. te Velde, F. M. Bickelhaupt, E. J. Baerends, C. Fonseca Guerra, S. J. A. van Gisbergen, J. G. Snijders and T. Ziegler, Chemistry with ADF, *J. Comput. Chem.*, 2001, **22**, 931–967.

30 ADF 2022.1, SCM, Theoretical Chemistry, ADF 2022.1, SCM, Theor. Chem. Vrije Univ. Amsterdam, Netherlands, https://www.scm.com.

31 J. P. Perdew, K. Burke and M. Ernzerhof, Generalized Gradient Approximation Made Simple, *Phys. Rev. Lett.*, 1996, **77**, 3865–3868.

32 Y. Zhang and W. Yang, Comment on "Generalized Gradient Approximation Made Simple", *Phys. Rev. Lett.*, 1998, **80**, 890.

33 E. Caldeweyher, S. Ehlert, A. Hansen, H. Neugebauer, S. Spicher, C. Bannwarth and S. Grimme, A generally applicable atomic-charge dependent London dispersion correction, *J. Chem. Phys.*, 2019, **150**, 154122.

34 E. van Lenthe, A. Ehlers and E.-J. Baerends, Geometry optimizations in the zero order regular approximation for relativistic effects, *J. Chem. Phys.*, 1999, **110**, 8943–8953.

35 S. Hirata and M. Head-Gordon, Time-dependent density functional theory within the Tamm–Dancoff approximation, *Chem. Phys. Lett.*, 1999, **314**, 291–299.

36 A. Klamt and V. Jonas, Treatment of the outlying charge in continuum solvation models, *J. Chem. Phys.*, 1996, **105**, 9972–9981.

37 S. F. Boys and F. Bernardi, The calculation of small molecular interactions by the differences of separate total energies. Some procedures with reduced errors, *Mol. Phys.*, 1970, **19**, 553–566.

38 M. Bouakil, A. J. Kulesza, S. Daly, L. MacAleese, R. Antoine and P. Dugourd, Visible Multiphoton Dissociation of Chromophore-Tagged Peptides, *J. Am. Soc. Mass Spectrom.*, 2017, **28**, 2181–2188.

39 J. M. Herbert, Visualizing and characterizing excited states from time-dependent density functional theory, *Phys. Chem. Chem. Phys.*, 2024, **26**, 3755–3794.

40 K. Harada, T. K. N. Nguyen, F. Grasset, C. Comby-Zerbino, L. MacAleese, F. Chirot, P. Dugourd, N. Dumait, S. Cordier, N. Ohashi, M. Matsuda and T. Uchikoshi, Light-dependent ionic-electronic conduction in an amorphous octahedral molybdenum cluster thin film, *NPG Asia Mater.*, 2022, **14**, 21.

41 M. H. Chisholm, Metal-metal bonds and metal-carbon bonds in the chemistry of molybdenum and tungsten alkoxides, *Polyhedron*, 1983, **2**, 681–722.

42 T. P. Second, J. D. Blethrow, J. C. Schwartz, G. E. Merrihew, M. J. MacCoss, D. L. Swaney, J. D. Russell, J. J. Coon and V. Zabrouskov, Dual-pressure linear ion trap mass spectrometer improving the analysis of complex protein mixtures, *Anal. Chem.*, 2009, **81**, 7757–7765.

43 B. G. Ward and F. E. Stafford, Synthesis and structure of four- and five-coordinated gaseous oxohalides of molybdenum(VI) and tungsten(VI), *Inorg. Chem.*, 1968, **7**, 2569–2573.

44 E. I. Stiefel, Progress in Inorganic Chemistry, *Prog. Inorg. Chem.*, 1977, **22**, 1–223.

45 L. S. Villata, M. R. Féliz and A. L. Capparelli, Photochemical and catalytic properties of dimeric species of molybdenum(V), *Coord. Chem. Rev.*, 2000, **196**, 65–84.

46 J. P. Murphy and R. A. Yost, Origin of mass shifts in the quadrupole ion trap: dissociation of fragile ions observed with a hybrid ion trap/mass filter instrument, *Rapid Commun. Mass Spectrom.*, 2000, **14**, 270–273.

47 J. E. McClellan, J. P. Murphy, J. J. Mulholland and R. A. Yost, Effects of Fragile Ions on Mass Resolution and on Isolation for Tandem Mass Spectrometry in the Quadrupole Ion Trap Mass Spectrometer, *Anal. Chem.*, 2002, **74**, 402–412.

48 A. Göbel, A. Rubio and J. Lischner, Light-Induced Charge Transfer from Transition-Metal-Doped Aluminum Clusters to Carbon Dioxide, *J. Phys. Chem. A*, 2021, **125**, 5878–5885.

23178 | *Phys. Chem. Chem. Phys.*, 2025, **27**, 23166–23178

This journal is © the Owner Societies 2025